One-Way Fluid-Structure Interaction Simulation of an Offshore Wind Turbine

Zhi-Kui Wang[1], Gwo-Chung Tsai[2, *], Yi-Bao Chen[3]

[1, 3]Department of Electromechanical and Automobile Engineering, Yan Tai University, Yantai, China.

[2]Department of Mechanical Engineering and Electromechanical Engineering, National I-Lan University, I-Lan, Taiwan, ROC.

Received 08 April 2014; received in revised form 28 April 2014; accepted 13 May 2014

Abstract

The Fluid-Structure Interaction (FSI) has gained great interest of scholars recently, meanwhile, extensive studies have been conducted by the virtue of numerical methods which have been implemented on wind turbine models. The blades of a wind turbine have been gained a deep insight into the FSI analyses, however, few studies have been conducted on the tower and nacelle, which are key components of the wind turbine, using this method. We performed the one-way FSI analysis on a 2-MW offshore wind turbine, using the Finite Volume Method (FVM) with ANSYS CFX solver and the RNG k-ε turbulence model, to achieve a comprehensive cognition of it. The grid convergence was studied and verified in this study, and the torque value is chosen to determine the optimal case. The superior case, which was chosen to conduct the FSI analysis, with a relative error is only 2.15%, thus, the accuracy of results is credible.

Keywords: fluid-structure interaction, offshore wind turbine, RNG k-ε turbulence model, grid convergence

1. Introduction

Energy dilemma has been occurred globally in recent decades. The traditional energy resources have experienced shortages dramatically, and the emission of exhaust gas caused by excessive consumption of fossil fuels has resulted in air pollution severely. Renewable energy, such as wind energy, solar energy, tidal energy and nuclear energy, has been adopted in some fields. Wind energy, which can be captured by wind turbines, has been acquired a relatively wide utilization by these machines. The wind turbine blades, which are made of composite materials, satisfies complicated design constraints, such as lower weight and proper stiffness, good resistance to the static and aerodynamic loading [1]. However, with the increasing size of the wind turbine blade, problems associated with it; for instance, structural strength, manufacturing and transportation difficulties have been occurred simultaneously [2]. A typical wind turbine fails 2.6 times during the first decade [3], and because of their continual operation, the rotor assembly was the most vulnerable component when compared with the gearbox and generator [4]. Thus, a lot of studies, such as one-way and two-way FSI analyses, have been conducted on the rotor to analyze it's structural properties.

The motion of the wind turbines is caused by a pressure differential between the two sides of blades, and research methods of the aerodynamic loading have gone through some transformations. The blade element momentum theory (BEM) was used in 1D codes which are quite simple and takes very short computational times as a point of departure, but they need

* Corresponding author. E-mail address: gctsai@niu.edu.tw
Tel.: +886-3-9357400; Fax: +886-3-9311326

experimental airfoil aerodynamic coefficients which are not easy to achieve [5]. The 3D computational fluid dynamics (CFD) numerical codes can solve the Navier-Stokes equations in detail with more realistically physical properties; however, long computational time and high quality of meshes is required simultaneously. The BEM transfers the aerodynamic loading into concentrated force and applies it to the blade surface; nevertheless, the pressure distribution on the blade surface cannot be reflected authentically. The 3D CFD numerical method has the advantage that surface pressure distribution can be obtained by the CFD software, and then loads the surface pressure into the mechanical system to calculate the structure properties, for example, stress, strain and deformation. This method is called one-way FSI analysis because only the data of fluid pressure acting at the structure is transferred to the structure solver and then being analyzed. For two-way FSI, the displacement of the structure is transferred to the fluid solver at the same time [6]. A non-matching fluid-structure interface discretization developed in [7] was used for FSI formulation. The partitioned approach-based non-conforming mesh method [3, 7] adopted in this paper can be divided into one-way and two-way FSI analyses. Grid convergence plays a crucial role in simulation software. Besides, Graf and Lukas [8] indicated that grid convergence studies were not typically conducted during the numerical investigation of large-scale real-world problems, since the simulation was quite time-consuming. Fine meshes show a subtle difference in results, however, coarse meshes require more integration points for large variations exist in the geometrical mapping [9]. Nabi and Khoury [10] indicated that a model converges on an accurate solution at a relatively coarse grid. Therefore, to conduct a grid convergence of a model is important.

This study focuses on the one-way FSI analysis of the offshore wind turbine, taking the aerodynamic pressure loading on the surface into consideration, and elaborating the process of load transfer from the fluid solver to the structural solver as well. The optimal case with the minimum relative error was validated and used to conduct this study, and the rational number of grids was determined, too.

2. Wind Turbine Model

2.1. Structure model and materials of the blade

The power curve of the offshore wind turbine, shown in Fig. 1, gives a definitely clear depiction of the relationship between wind speed and electrical power. Fig. 1 shows that the rated wind speed is 15m/s, and the cut-in and cut-out wind speed is 3 m/s and 25 m/s, respectively. Fig. 2(a) depicts the wind velocity, which is given by Eq. (1), varies with time. The initial wind velocity at hub height is 10 m/s, and the periodic of the wind is about 20.5s. The maximum wind velocity value occurs at 5.2 s, with the value is close to 15 m/s. Fig. 2(b) indicates that the maximum rotor angular velocity is 20 r/min which occurs at 5.2 s as well. The relationship of the wind speed and rotor angular velocity is given by Eq. (1) and Eq. (3) [11].The structure of a wind turbine is mainly divided into four key components: the blade, hub, nacelle and tower. The blade, which is made of composite materials to achieve a higher specific strength and specific stiffness, has been gained a comprehensive study of FSI analyses to achieve the mechanical properties, such as surface pressure distribution, stress and strain [12-14]. The Tower and nacelle, which are key components of an offshore wind turbine, to the best of best knowledge, they gained few studies these years. Table 1 shows the properties of the composite material DL900 which are used for used for the blade, and the density of it is 1900 kg/m^3. Other components use the materials of structural steel. We substituted D (D=85 m) for both the rotor diameter and the rotor domain (Inner flow field domain), and the diameter of the rotor domain equals to the rotor diameter.

Table 1 Mechanical properties of the composite materials for blade

L900	EX	EY	EZ	GXY	GXZ	GYZ	PRXY	PRXZ	PRYZ
	32.8 GPa	9.56 GPa	9.56 GPa	3.9 GPa	3.1 GPa	3.1 GPa	0.258	0.129	0.129

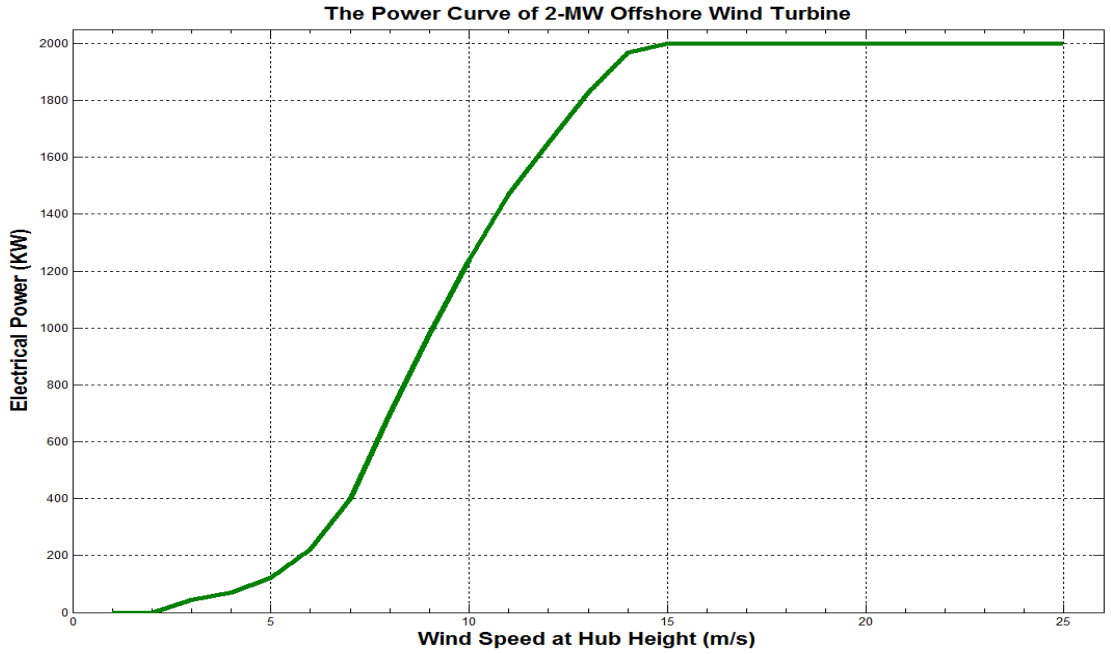

Fig. 1 Power curve of the offshore wind turbine

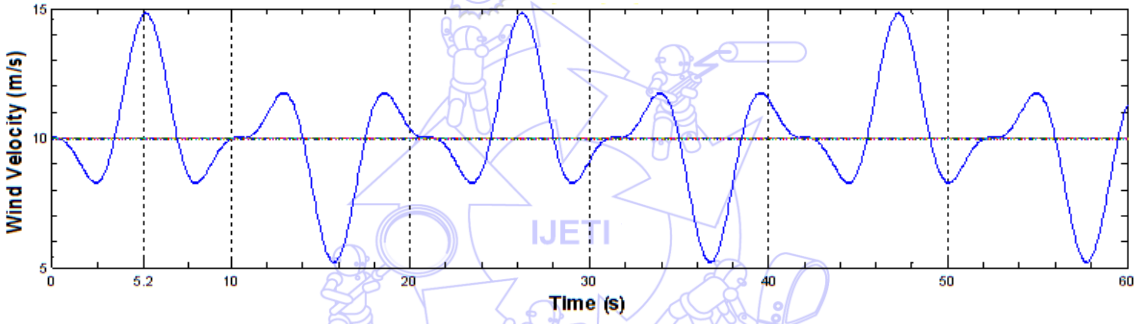

(a) Wind velocity changing over time

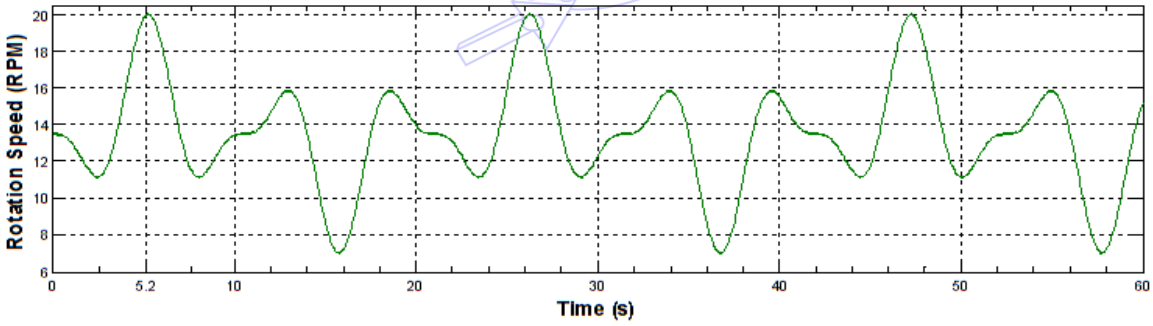

(b) Rotational speed changing over time

Fig. 2 Gust wind speed and rotor angular velocity varying with time

The function of the wind speed is expressed as follows:

$$V(z,t)=\begin{cases} V(z)-0.37V_{gust}\sin(3\pi t/T)(1-\cos(2\pi t/T)) & for\ 0\le t\le T \\ V(z) & otherwhise \end{cases} \quad (1)$$

Where V(z) is the wind speed at hub height, V_{gust} is the gust wind speed and detail denotation is given in [11]. T is the gust characteristic time 10.5 s, which is given in [11] as well.

The tip-speed ratio is defined as the ratio between the linear blade tip speed and wind velocity, and is written as follows:

$$\lambda = \frac{R\omega_R}{V_H} \tag{2}$$

$$\omega_R = \frac{\lambda V_H}{R} = \frac{2\lambda V_H}{D}\left(\frac{rad}{s}\right) \rightarrow n = \frac{2\lambda V_H}{D}\frac{60}{2\pi}(r/\min) = \frac{60\lambda V_H}{\pi D}(r/\min) \tag{3}$$

What we chose the tip-speed ratioλ=6, ω_R is the angular velocity of the rotor, D denotes the rotor diameter, n is the rotational angular velocity, and V_H represents the wind speed here.

2.2. *Flow field model*

Designing a reasonable flow field domain is significant to the CFD analysis. Creating a smaller flow field which is used to domain used to conduct this analysis could not obviate the effect of wake effects. However, if it was colossal then it might generate redundant number of cells, and increase the computational time. The ANSYS Design Modeler application's geometry engine has a one cubic kilometer size box limitation, centered about the world origin [15]. Taking the dimensions' ratio of the flow field domain design [13] into account, we create the out flow field domain with a length: width: height ratio is 7D: 5D: 2D (D presents the rotor diameter, 85m), which is shown in Fig. 3. The boundary conditions (BC) were defined as follows: a transient analysis with total time 21s and time step 0.01s were defined in the analysis type; a frozen rotor type of the Rotor domain, which can be used for axial compressors and turbines, used as the rotor as it changes the reference frame while maintaining the relative position of the components; the left face of the outer flow field domain was defined as the Wind (Inlet) BC, and the inlet velocity denoted as the V(z,t) in Eq. (1) is defined by the CFX Expression Language (CEL); the right face of it was used as the Outlet BC, and the opening boundary condition, which allows the fluid to cross the boundary surface in either direction, was adopted; Symmetry BC were used for the lateral surface because it can reduce the size of the outer flow field domain and eliminate the real wall effects; the no slip wall was applied at the bottom wall of the flow field.

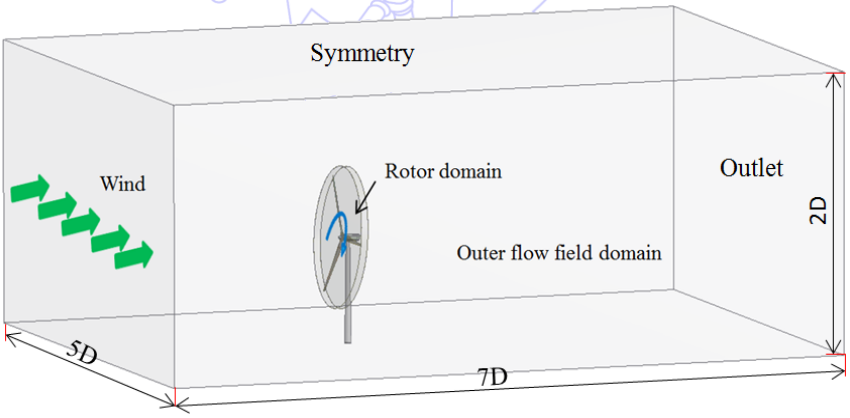

Fig. 3 Computational fluid dynamic domain

2.3. *Grid convergence*

Achieving the accuracy of results for a flow field domain is of vital importance. The accuracy of results and the reasonable number of grid cells need striking a balance. The number of grid cells dominates the efficiency of computational time. Hence, conducting the study of grid convergence is necessary and significant. As far as we know, Lanzafame [5] converted the mesh from tetrahedral to polyhedral geometry in order to reduce grid numbers and Wang and Zhan [16] performed only five cases on the total dynamic torque coefficient to achieve the optimal grid number. Though grid convergence was conducted by

these scholars with different methods, more cases should be conducted to achieve the finest grid cells. We conducted gird convergence study on nine cases shown in Table 2, using the torque, power and relative error to verify the results of the wind turbine. The formulation of power and torque is written as

$$P = \frac{T \cdot n}{9550} \tag{4}$$

where P (KW) is the electrical power; T (N·m) is the torque of wind turbine, n (r min^-1) is the rotational velocity.

Table 2 The simulation results and relative error of different cases

Cases	Torque（N·m）	Power (MW)	Relative error (%)
Case_1	322968	0.676	66.2
Case_2	1745300	3.655	82.75
Case_3	1811540	3.794	89.7
Case_4	984782	2.062	3.1
Case_5	975499	2.043	2.15
Case_6	909347	1.904	4.8
Case_7	840529	1.76	12
Case_8	770835	1.614	19.8
Case_9	904009	1.893	5.35

The Equations of dynamic torque coefficient C_T and power coefficient C_P are defined as

$$C_T = \frac{T}{(1/2)\rho RSV^2} \tag{5}$$

$$C_P = \frac{P}{(1/2)\rho SV^3} = \frac{T}{(1/2)\rho RSV^2 R}\frac{R\varpi}{V} = C_T\lambda \tag{6}$$

Where the unit of P (power of the rotor) in Eq. (6) is watt; T is the dynamic torque; ρ denotes the density of air, 1.225 kg/m^3; V is the wind velocity; R is the radius of the rotor domain, and S represents the swept area (5674.5 m^2); ω is the rotor angular velocity.

The relative error which is given by Eq. (7) is the absolute error divided by the magnitude of the exact value (rated power, 2MW).

$$E_R = \frac{|P - P_R|}{P_R} \times 100\% \tag{7}$$

where E_R indicates the relative error; P and P_R denote the power calculated by Eq. (4) in these simulations and the rated power, respectively.

Table 2 shows nine cases clearly above, and case_5 is the best case whose relative error is only 2.15%.To achieve an explicit description of the grid cells among the nine cases, Table 3 is given to validate the grid convergence. It is cushy to notice from Table 3 that the mesh converged with approximately 1.025×10^6 total grid cells.

Table 3 The grids number of different cases

Cases	Total grids		Outer flow field grids		Rotor flow field grids	
	Nodes	Elements	Nodes	Elements	Nodes	Elements
Case_1	11650	6917	6421	3704	5229	3213
Case_2	78456	49052	35308	20643	43148	28409
Case_3	502592	347132	401295	279589	101297	67543
Case_4	126480	672015	78605	418638	47875	253377
Case_5	194992	1025009	90068	464934	104924	560075
Case_6	233831	1245885	124392	648165	109439	597720
Case_7	301645	1602014	148412	770811	153233	831203
Case_8	353878	2030036	344508	1982599	9370	48437
Case_9	533225	2984699	424015	2388061	109210	596638

2.4. Numerical methods

The RNG k-ε turbulence model which was proposed by Yakhot et al. [17], using a rigorous statistical technique: renormalization group theory. The transport equation is given by Eq. (8). It has certain advantages when compared with the standard *k*-ε model, such as, improving the accuracy for rapidly strained flows significantly, enhancing accuracy for swirling flows, and providing an analytically-derived differential formula for low-Reynolds-number effects. Nonetheless, the RNG *k*-*ε* model seems to take 10-15% more CPU time than the standard *k*-*ε* model on account of the extra terms and functions in the governing equations and a greater degree of nonlinearity [18]. All these relative equations are discretized with the FVM, using a Second Order Upwind scheme.

$$\frac{\partial(\rho\varepsilon)}{\partial t}+\frac{\partial}{\partial x_j}(\rho U_j\varepsilon)=\frac{\partial}{\partial x_j}\left[\left(\mu+\frac{\mu_t}{\sigma_{\varepsilon RNG}}\right)\frac{\partial\varepsilon}{\partial x_j}\right]+\frac{\varepsilon}{\kappa}\left(c_{\varepsilon 1RNG}p_\kappa-c_{\varepsilon 2RNG}\rho\varepsilon+c_{\varepsilon 1RNG}p_{\varepsilon b}\right) \tag{8}$$

Where the RNG k-ε turbulence model coefficient $c_{\varepsilon 1RNG}$ is written as

$$c_{\varepsilon 1RNG}=1.42-f_\eta \tag{9}$$

Details of these symbols used in Eq. (8) and Eq. (9) can be found in [18].

The node-projection (N-P) schemes, which is one of methods used to transfer the fluid traction to the structural mesh surface, was analyzed comprehensively by Farhat et al. [19] and used in our study. The N-P scheme illustrated in Fig. 4 projects the fluid nodes onto the structural surface element to extract the load vector on the solid interface nodes. The extracted load vector on the structural surface node is written [19, 20] as

$$F_s^{\ j}=\sum_{i=1}^{m_f}N_s^{\ j}(x^i)F_f^i \tag{10}$$

Where F_s^j is the discrete value of F_s at the fluid point j, F_f^i is the discrete value of F_f at the structure node i; N_s^j denotes the standard finite element shape function, associated with node j of the structural interface mesh and m_f is the number of structure nodes on the structural interface meshes; x_i denotes the location of node i of the fluid interface mesh.

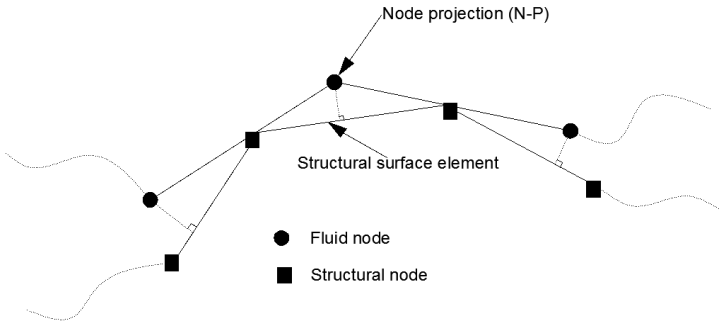

Fig. 4 Node-projection scheme for load transfer

3. Results and Discussion

The FSI analysis was conducted on the offshore wind turbine, especially the results of the blade, were given a comparison with other scholar's study. Moreover, the other components of the wind turbine were analyzed and discussed in the meantime. As we set up the time-step 0.01 s, and the output frequency option in the output control is set "Every Time-step". According, it yields a corresponding result each time-step. However, conducting the analyses for each time-step is unpractical and time-consuming as we set up the total time 21 s, therefore, 5.2 s was chosen to perform the study because the maximum wind speed is close to the rated speed value. Fig. 5 shows the surface pressure distribution and mechanical properties of the blade.

Fig. 5(a) shows the surface pressure distribution of one of the three blades in CFX solver, and Fig. 5(b) depicts the equivalent pressure distribution of it in Structure solver. Comparing the surface pressure distribution in Fig. 5(a) and Fig 5(b), both of them achieve the agreement that a larger surface pressure value occurs at the tip of the blade. However, the pressure legend in Fig. 5(a) indicates that the surface pressure has positive and negative values, while only positive values occurs in Fig. 5(b). The fluid domains were calculated with FVM in CFX solver, using the optimal case with the rational grid cells. Thus, we generated a relatively matching mesh in the Structural solver to guarantee the data exchange of loads between these two solvers. The positive pressure values which is in CFX solver are changed into tension in Structural solver while negative pressure values turn into compressive stress. The Structure solver, using the node-projection scheme to map the load, does not distinguish properties (positive or negative) of values. Consequently, all their values in the structural solver turn into positive. The main difference lies in the direction: tension is perpendicular to the surface and towards the outer, on the other hand, compressive stress is towards the inner with the direction perpendicular to the surface.

Fig. 5(c) and Fig. 5(d) show the distribution of stress and strain of the blade. Fig. 5(c) indicates that the main stress of the blade is located away from 70% to 90% of the root, and the strain distribution is similar to it. The results in Fig. 5(d) have an agreement with the study of Chen *et al.* [1], and we can conclude that the results are credible. Two reasons were pointed out by Chen to explain it:

(1) The normal operation that used the rated wind speed had less impact on the strength of the root than the limited load condition.

(2) The surface pressure applied on the blade finite element model directly rather than translate the surface pressure into concentrated load.

Another reason we deemed it should also be considered is that the surface pressure directions have changed in the data translating process, and the mapping of data between these two solvers could not be absolutely accurate, which resulted in the

unevenness of pressure.

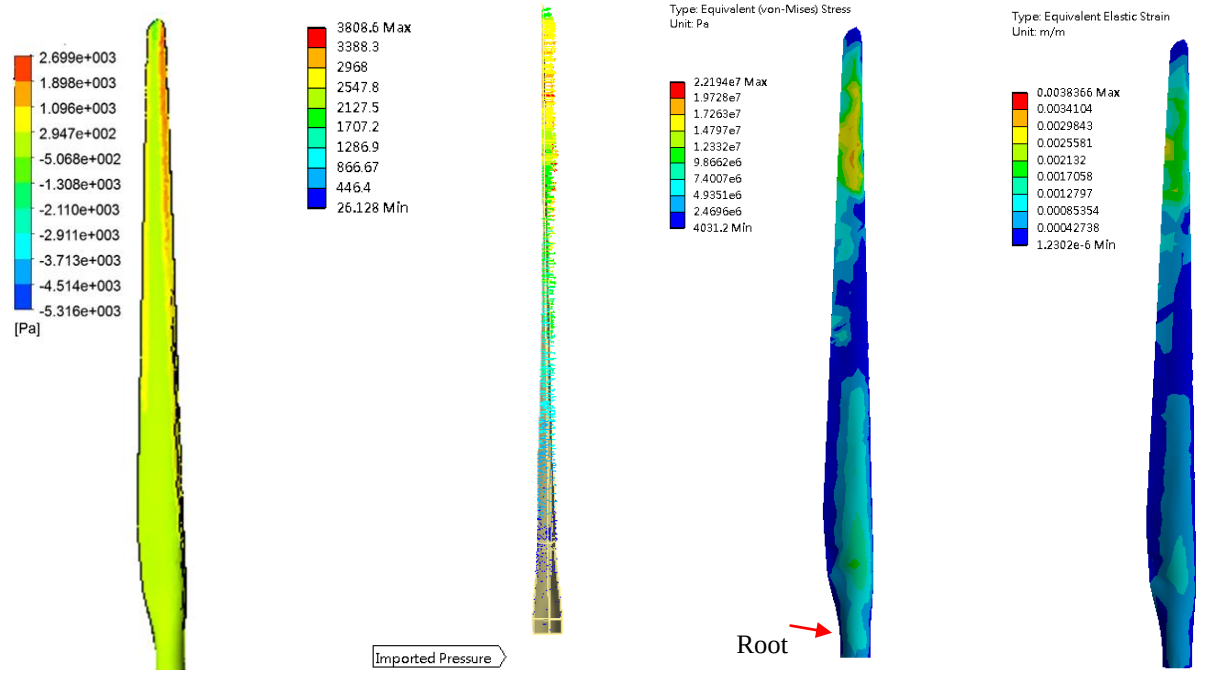

(a) Surface pressure distribution in CFX

(b) Surface pressure distribution in Structure

(c) Equivalent stress of the blade

(d) Equivalent strain of the blade

Fig. 5 Surface pressure distribution and mechanical stress and strain of the blade

Fig. 6 depicts the maximum stress and strain which locate at the junction of the blade and hub. In this paper, gravity and inertial force which have a crucial effect on the analysis are taken into account. Thus, moments of the blades are very large especially when the length of the blade performed in this study is long. The stress concentration always occurs at some positions, such as the sharp corners, holes, notches and grooves. The junction of the blade and hub is a sharp corner, that is the reason why the maximum stress occurs at this positions. Considering all these factors, the maximum value occurs at this location is rational.

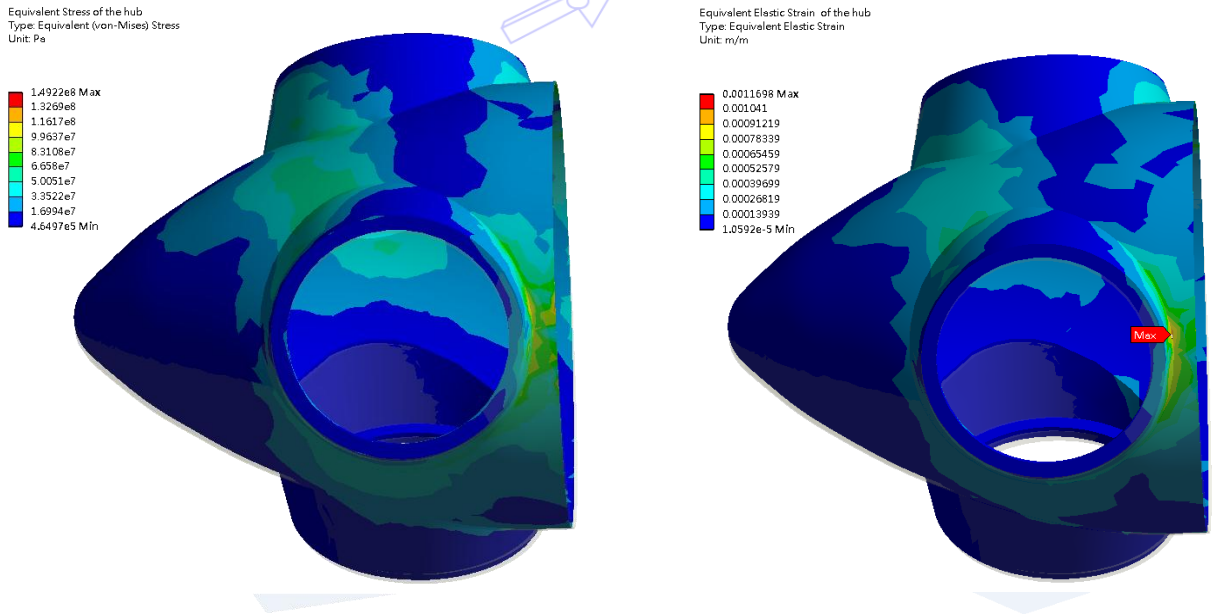

(a) Equivalent stress of the hub

(b) Equivalent strain of the hub

Fig. 6 Mechanical properties of the hub

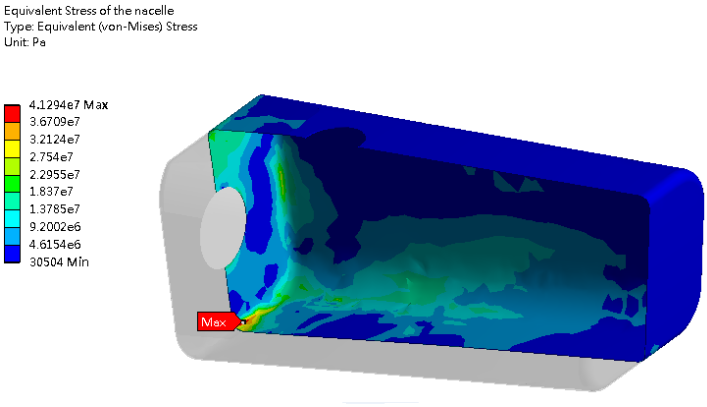

(a) Equivalent stress of the nacelle

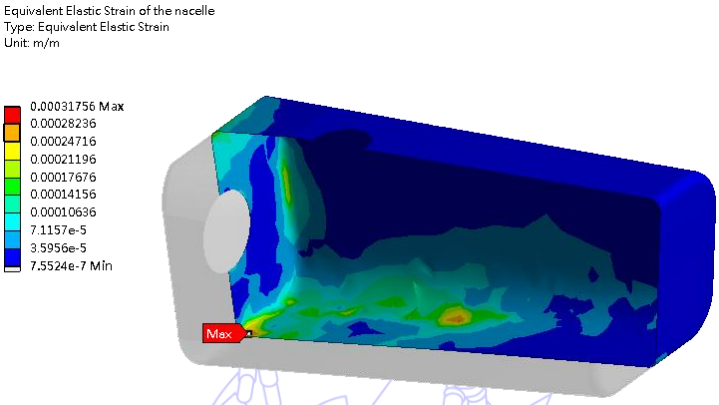

(b) Equivalent strain of the nacelle

Fig. 7 Mechanical properties of the nacelle

Fig. 7 indicates that the main stress and strain are situated in the lower part of the front of the nacelle. The nacelle is supported with the tower, and it is fixed with the tower. However, the tower is fixed to the ground regardless of how much the wind velocity (typhoon may be not included) is. The swept area S is large, besides the surface pressure on these blades generates a considerable pressure which loads on the front side of the nacelle. The front side of the nacelle withstands the pressure from both the pressure of the rotor and the hub. Therefore, a larger stress and strain occurred in these corners, where stress concentration lies.

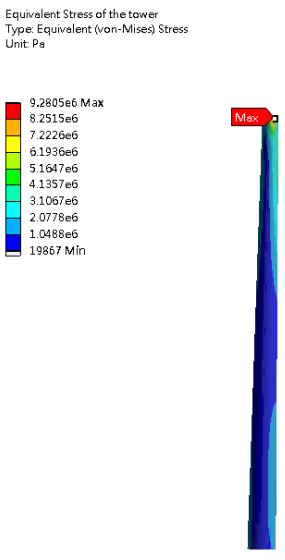

(a) Equivalent stress of the tower

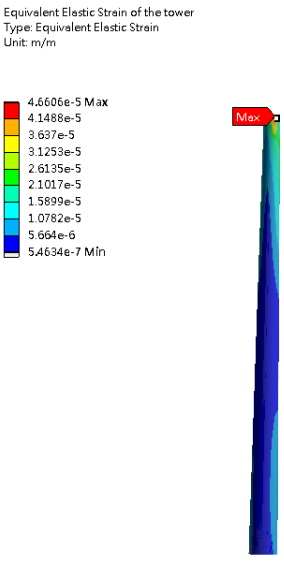

(b) Equivalent strain of the tower

Fig. 8 Mechanical properties of the tower

4. Conclusions

In this study, the FSI analysis with a numerical simulation was conducted on the offshore wind turbine, and the results of the FSI were analyzed in some degree. The main conclusions of this study are listed below.

(1) The one-way FSI analysis was conducted on the full machine, using the FVM and RNG k-ε turbulence model, to achieve the mechanical properties of the offshore wind turbine. The data exchang process between CFX solver and Structural solver was analyzed as well.

(2) Grid convergence has critical effects on the accuracy of results and computational time. However, few studies on the offshore wind turbine have been conducted. In this study, the grid convergence was analyzed and verified with several cases. The case, which was verified as the optimal case, was determined and used to conduct the FSI analysis. Thus, the results achieved in these analyses with the minimum relative error are credible.

(3) The mechanical properties of the offshore wind turbine, such as stress and strain, were studied for the full machine. The strain of the blade was compared with other scholar's results, and gains a good agreement with it. Other components, such as the hub, nacelle and tower, were given a comprehensive analysis on its mechanical properties as well.

Acknowledgements

The authors wish to thank the Ministry of Science and Technology of the Republic of China for the grant under project #MOST 103-3113-E-002-003, which makes this research possible.

References

[1] J. Chen, Q. Wang, W. Z. Shen, X. Pang, S. Li, and X. Guo, "Structural optimization study of composite wind turbine blade," Materials & Design, vol. 46, pp. 247-255, 2013.
[2] Y. J. Lee, Y. T. Jhan, and C. H. Chung, "Fluid–structure interaction of FRP wind turbine blades under aerodynamic effect," Composites Part B: Engineering, vol. 43, pp. 2180-2191, 2012.
[3] Y. Bazilevs, M. C. Hsu, I. Akkerman, S. Wright, K. Takizawa, B. Henicke, et al., "3D simulation of wind turbine rotors at full scale. Part I: Geometry modeling and aerodynamics," International Journal for Numerical Methods in Fluids, vol. 65, pp. 207-235, 2011.
[4] E. Echavarria, B. Hahn, G. J. W. van Bussel, and T. Tomiyama, "Reliability of wind turbine technology through time," Journal of Solar Energy Engineering, vol. 130, pp. 031005, 2008.
[5] R. Lanzafame, S. Mauro, and M. Messina, "Wind turbine CFD modeling using a correlation-based transitional model," Renewable Energy, vol. 52, pp. 31-39, 2013.
[6] F. K. Benra, H. J. Dohmen, J. Pei, S. Schuster, and B. Wan, "A Comparison of one-way and two-way coupling methods for numerical analysis of fluid-structure interactions," Journal of Applied Mathematics, vol. 2011, pp. 1-16, 2011.
[7] Y. Bazilevs, M. C. Hsu, and M. A. Scott, "Isogeometric fluid–structure interaction analysis with emphasis on non-matching discretizations, and with application to wind turbines," Computer Methods in Applied Mechanics and Engineering, vol. 249-252, pp. 28-41, 2012.
[8] T. Graf and L. Degener, "Grid convergence of variable-density flow simulations in discretely-fractured porous media," Advances in Water Resources, vol. 34, pp. 760-769, 2011.
[9] T. J. R. Hughes, J. A. Cottrell, and Y. Bazilevs, "Isogeometric analysis: CAD, finite elements, NURBS, exact geometry and mesh refinement," Computer Methods in Applied Mechanics and Engineering, vol. 194, pp. 4135-4195, 2005.
[10] M. Nabi and R. Al-Khoury, "An efficient finite volume model for shallow geothermal systems—Part II: Verification, validation and grid convergence," Computers & Geosciences, vol. 49, pp. 297-307, 2012.
[11] Internal Electrotechnical Commission, International Stanard IEC 61400-1 wind turbines-part 1: Design requirements, 3rd ed. Switzerland: Geneva, 2005.
[12] M. C. Hsu and Y. Bazilevs, "Fluid–structure interaction modeling of wind turbines: simulating the full machine," Computational Mechanics, vol. 50, pp. 821-833, 2012.

[13] Y. Bazilevs, M. C. Hsu, J. Kiendl, R. Wüchner and K. U. Bletzinger, "3D simulation of wind turbine rotors at full scale. Part II: Fluid-structure interaction modeling with composite blades," International Journal for Numerical Methods in Fluids, vol. 65, pp. 236-253, 2011.
[14] J. M. M. Monteiro, J. C. Páscoa, and F. M. R. P. Brojo, "Simulation of the Aerodynamic Behaviour of a Micro Wind Turbine," International Conference on Renewable Energies and Power Quality, Apr. 2009.
[15] F.W. Li, Introduction of air and gas dynamics. Northwestern Polytechnical University Press, 1st ed. China: Shan Xi- Xi An, May 2007.
[16] Y. F. Wang and M. S. Zhan, "3-Dimensional CFD simulation and analysis on performance of a micro-wind turbine resembling lotus in shape," Energy and Buildings, vol. 65, pp. 66-74, 2013.
[17] V. Yakhot, S. Thangam, T.B. Gatski, S.A. Orszag and C.G. Speziale, "Development of turbulence models for shear flows by a double expansion technique," Physics of Fluids A: Fluid Dynamics, vol. 4, no. 7, pp. 1510-1520, 1992.
[18] ANSYS, Inc., ANSYS mechanical APDL theory reference. ANSYS, Inc., USA, 2012.
[19] R. K. Jaiman, X. Jiao, P. H. Geubelle, and E. Loth, "Conservative load transfer along curved fluid–solid interface with non-matching meshes," Journal of Computational Physics, vol. 218, pp. 372-397, 2006.
[20] C. Farhat, M.Lesoinnea, and P. LeTallecb, "Load and motion transfer algorithms for fluids structure interaction problems with non-matching discrete interfaces: momentum and energy conservation, optimal discretization and application to aeroelasticity," Computer Methods in Applied Mechanics and Engineering, vol. 157, no. 1-2, pp. 95-114, April 1998.